Three-Dimensional Deconvolution of Wide Field Microscopy with Sparse Priors: Application to Zebrafish Imagery

Bo Dong, Ling Shao
Department of Electronic and Electrical Engineering
The University of Sheffield
Email: bdong2@sheffield.ac.uk, ling.shao@sheffield.ac.uk

Alejandro F Frangi
Department of Mechanical Engineering
The University of Sheffield
Email: a.frangi@sheffield.ac.uk

Oliver Bandmann, Marc Da Costa
Department of Neuroscience
The University of Sheffield
Email: o.bandmann@sheffield.ac.uk, m.dacosta@sheffield.ac.uk

***Abstract*—Zebrafish, as a popular experimental model organism, has been frequently used in biomedical research. For observing, analysing and recording labelled transparent features in zebrafish images, it is often efficient and convenient to adopt the fluorescence microscopy. However, the acquired z-stack images are always blurred, which makes deblurring/deconvolution critical for further image analysis. In this paper, we propose a Bayesian Maximum a-Posteriori (MAP) method with the sparse image priors to solve three-dimensional (3D) deconvolution problem for Wide Field (WF) fluorescence microscopy images from zebrafish embryos. The novel sparse image priors include a global Hyper-Laplacian model and a local smooth region mask. These two kinds of prior are deployed for preserving sharp edges and suppressing ringing artifacts, respectively. Both synthetic and real WF fluorescent zebrafish embryo data are used for evaluation. Experimental results demonstrate the potential applicability of the proposed method for 3D fluorescence microscopy images, compared with state-of-the-art 3D deconvolution algorithms.**

I. Introduction

Zebrafish has been used as an important model organism for many kinds of disease research, such as cancer and Parkinson's disease. Zebrafish is extremely useful to scientists, because this kind of fish is vertebrate with an immune system highly similar to human beings. In addition, zebrafish embryos develop externally and are transparent providing an unparalleled opportunity to study the biology of the immune response. Compared to image analysis of tissue samples from other species, such as mice or humans, where slides with clearly orientated tissue samples of well-defined, standardized thickness would typically form the basis of any subsequent image acquisition and analysis, whole mount *in situ* staining or immunohistochemistry of zebrafish embryos results in the challenge of having to undertake image analysis in a tissue sample of ill-defined height and orientation.

Zebrafish embryos are observed using light Microscopy, which has been fundamental in advancing our understanding of the molecular and cellular biology of health and diseases. Particularly, WF Fluorescence Microscopy is conventional, and widely used for observing, analysing and imaging specific labelled features of small living specimens. Compared with the confocal microscopy, WF microscopy is much faster and more convenient, which can also record the information of the whole specimen and make the high throughput imaging and large-scale image analysis possible. The current usefulness of zebrafish for high throughput screens is limited due to high variability in signal strength and signal distribution within particular regions of interest of the transparent zebrafish body. These are at least partially due to technical problems whilst embedding the zebrafish embryos for subsequent image analysis but also due to the specific nature of image acquisition in zebrafish.

During the light illumination, both focus and out-of-focus lights are recorded by the Charge-Coupled Device (CCD) camera. To use recorded images for further research, (such as feature detection, cell tracking and cell counting), the out-of-focus light in the z-stack images should be removed first. According to [1], the imaging process using WF or confocal fluorescence microscopy is assumed to be linear and shift invariant. Then, the whole imaging process can be seen as a 3D convolution process. In this paper, we focus on the 3D WF fluorescent images. The 3D fluorescent information of the specimens will be recorded as a z-stack of images. The inverse procedure, *i.e.*, removing the out-of-focus light in z-stack images, is known as 3D deconvolution. The convolution process can be formulated as:

$$g(x) = n(\sum_{k \in \Omega \subset \mathbb{R}^3} h(k) f(x-k)), \tag{1}$$

where
g : observed, blurred image,
$h : \mathbb{R}^3 \to \mathbb{R}$–point spread function of the imaging system,
$f : \mathbb{R}^3 \to \mathbb{R}$–latent image or ground truth image function,
n : voxelwise noise function,
$\Omega : \Omega \subset \mathbb{R}^3$ is the support in the specimen domain recorded by the imaging system,
x : 3-tuple of discrete spatial coordinates.
Equation (1) can be written in a short form:

$$g = n(h * f), \tag{2}$$

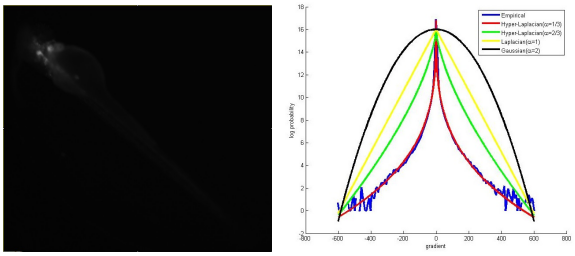

(a) One frame of the stack (b) log-gradient distribution

Fig. 1: (a) is one frame of a zebrafish embryo z-stack. (b): The blue curve describes the gradient distribution ($\bigtriangledown_x f$) of the image. The Hyper-Laplacian with $\alpha = 1/3$ is a more appropriate model to describe the log-gradient distribution (blue), compared with the Gaussian (black), Laplacian (yellow) or Hyper-Laplacian with $\alpha = 2/3$ (green) log-distribution.

where $*$ is the 3D convolution operator.

The convolution kernel h is called Point Spread Function (PSF), which describes the blurring shape of one point light through the light microscope [2]. In this paper, the PSF is calculated using an analytical model if the true PSF is not given, which is called the Variable Refractive index Gibson and Lanni (VRGL) model [3]. The final goal of the deconvolution method is to estimate the best latent image from the observed image with the given PSF. During the imaging process, the fluorescent data are influenced by photon noise, which can be described as a Poisson distribution [4]:

$$p(k) = \frac{\lambda^k e^{-\lambda}}{k!}, k = 0, 1, 2, ... \quad (3)$$

In this paper, the MAP method with sparse image priors, including the Hyper-Laplacian prior and a local prior with mask, is presented to solve the 3D deconvolution problem for WF Fluorescence Microscopy images. Then, the proposed method is tested on both synthetically generated microscopy data and real WF microscopy data from zebrafish. Compared with other regularization methods, the unique part of the proposed method is that we combine the Hyper-Laplacian model and a local mask together into the MAP framework for 3D deconvolution.

The main contributions of our work include three aspects. Firstly, the MAP method with sparse priors is applied to 3D deconvolution for Poisson noise WF microscopy images. Secondly, the Hyper-Laplacian distribution as a global prior is used in the deconvolution framework. The Hyper-Laplacian distribution is a better model to describe the log-gradient distribution of the image compared with other models, especially for WF microscopy images. Finally, a local mask as the second prior is applied to the 3D deconvolution problem for reducing ringing artifacts.

The structure of this paper is as follows. In the next section, a brief review of relevant works is given. Section 3 explains how sparse priors are designed in the MAP framework for Poisson noise WF images, and also describes the VRGL model for generating PSF. Section 4 gives the experimental results using three different datasets. In section 5, we conclude the paper.

II. Related Works

Deconvolution is a typical area in image restoration [5], [6]. Traditional methods such as inverse filtering [7], Tikhonov filtering [8], Weiner filtering [9], and Richardson-Lucy algorithm [10], [11] were proposed several decades ago for the inverse problem. A non-linear iterative method, Maximum Likelihood Expectation Maximization (MLEM), which is similar to the Richardson-Lucy algorithm, has been designed for solving both the blind and the non-blind Poisson image deconvolution problems [12], [13], [14], [15]. A machine learning method modelling the PSF based on MLEM was introduced for blind deconvolution [15]. Most of the inverse problems are ill-posed, and the 3D deconvolution problem is also no exception. Therefore, the observed image (g) can be explained using infinite pairs of the PSF (h) and the ground truth image (f) [16]. Several methods using the Maximum a-Posteriori (MAP) estimation approach with the sparse image prior for solving the two-dimensional (2D) deconvolution problem were presented [16], [17], [18].

The MAP approach, as a non-linear iteration method, was proved to be very efficient and accurate to recover the true blur kernel of the 2D image, due to the movement of the object or the shake of the camera [16]. The sparse derivative distribution, as a kind of image prior knowledge, has been used for solving many ill-posed problems, such as motion deblurring [19], denoising [20], transparency separation [21] and super resolution [22].

In Fig. 1, the empirical distribution (blue) is the log-probability of the image gradient, and this heavy-tailed distribution is known as the sparse image prior. State of the art estimation strategies for demonstrating the sparse prior model were proposed, including using the Tikhonov-Miller regularizer [23] and the Total Variation (TV) regularization [13], [14], which will be used for comparison in this paper. Different penalty functions were introduced for the gradient filter, such as $f_1(x) = |\bigtriangledown x|$ for the TV regularization method and $f_1(x) = \|\bigtriangledown x\|^2$ for the TM regularization method [13]. The Total variation regularization term was applied to 3D deconvolution for microscopy data [13]. In [14], the TV regularization term was presented for blind iterative deconvolution by updating both the latent image function and the PSF simultaneously.

The Hyper-Laplacian distribution has been applied to 2D non-blind deconvolution [24]. In [18], the Hyper-Laplacian distribution was modified with the Gaussian noise model, and a lookup table (LUT) was developed for improving the computational speed. In [17], both global and local priors were introduced for solving the motion deblurring problem from a single image. For the global prior, they presented two piecewise continuous functions to fit the heavy-tailed distribution. The local prior was used for suppressing ringing artifacts. Our local prior part is similar to the method in [17].

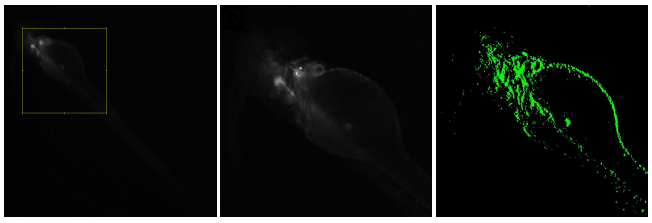

(a) Original frame (b) Zoom-in of the yellow box in (a) (c) The smooth regions Ψ are shown in black and texture regions are highlighted in green

Fig. 2: (a): One frame of an original zebrafish z-stack; (b): Zoom-in of the yellow box in (a); (c): After applying the triangle threshold to the image g_x. The green color indicates texture regions of the image, and the remaining part is Ψ.

III. Deconvolution Framework

In this section, a Maximum a-Posterior algorithm with sparse priors is presented for estimating the best latent image f given the blurred image g and the PSF h. According to the Bayes Rule:

$$p\left(f|g,h\right)=\frac{p\left(g|f,h\right)p\left(f\right)}{p\left(g\right)}\propto p\left(g|f,h\right)p\left(f\right), \tag{4}$$

where $p\left(f\right)$ is a prior about f, $p\left(g|f,h\right)$ can be seen as a Poisson distribution with mean $\left(f*h\right)(x)$, and Equation (3) can be rewritten as:

$$p\left(g\left(x\right)|f,h\right)=\frac{\left(f*h\right)\left(x\right)^{g(x)}e^{-(f*h)(x)}}{g\left(x\right)!}. \tag{5}$$

The sparse image priors will be discussed in the following subsections.

A. Sparse Image Priors

In this paper, to simultaneously address the ill-posed nature of the problem and ringing artifacts reduction when restoring the latent image f, the prior $p(f)$ is decomposed into two components, including a global prior $p_g\left(f\right)$ [18] and a local prior $p_l\left(f\right)$ [17]:

$$p\left(f\right)=p_g\left(f\right)p_l\left(f\right). \tag{6}$$

1) Global Prior $p_g\left(f\right)$: The heavy-tailed distribution of the gradient in the WF fluorescence microscopy z-stack is explained well by the Hyper-Laplacian distribution [18]. In Fig. 1, it can be seen that the best approximation for the logarithmic image gradient distribution is the Hyper-Laplacian distribution with $\alpha=1/3$. The global prior $p_g\left(f\right)$ is defined as:

$$p_g\left(f\right)\propto\prod_{i\in\Omega\subset\mathbb{R}^3}e^{-\tau|\bigtriangledown f_i|^\alpha},(0<\alpha<1), \tag{7}$$

where τ is the positive rate parameter, and $\bigtriangledown$ is the 3D first order derivative filter.

2) Local Prior $p_l\left(f\right)$: Besides the global prior, a local prior with mask is used for reducing ringing artifacts, which was introduced first in a motion deblurring problem [17]. In this paper, we design a similar local prior for 3D deconvolution, but the difference is that we use a triangle threshold method [25] to determine the smooth region in the z-stack images automatically. It is indicated in [17] that the smooth region in the image should also be smooth after restoration, and this local prior can suppress ringing artifacts effectively in both the smooth regions and the texture regions. Due to the inaccurately generated PSF, some ringing artifacts will appear near the boundary and the edges after a number of iterations during the restoration in the frequency domain. Similar to [17], the error of the gradient between the estimated image and the blurred image in the smooth area is defined to follow the Normal distribution with zero mean:

$$p_l\left(f\right)=\prod_{i\in\Phi}N\left(\bigtriangledown f_i-\bigtriangledown g_i|\,0,\sigma\right), \tag{8}$$

where Φ denotes the smooth regions in each frame of the z-stack images, and the smooth regions Φ are shown in Fig. 2. Even though this local prior is only defined in the smooth regions, it can globally reduce ringing artifacts due to the effect of the PSF during the restoration [17]. We define a mask function, $M(x)$, to describe the smooth regions Ψ in the z-stack images. The triangle threshold algorithm [25] is applied to determine the threshold automatically, and Ψ indicates the regions where $M(x)=1$:

$$M(x)=\begin{cases}0, & g\geq Threshold\\ 1, & else.\end{cases} \tag{9}$$

B. Optimization

After defining the two priors, Equation (4) becomes:

$$p\left(f|g,h\right)\propto p\left(g|f,h\right)p_g\left(f\right)p_l\left(f\right). \tag{10}$$

Instead of maximizing the likelihood probability of Equation (10), the negative log-likelihood function, $J(f)$, is minimized. In the function $J(f)$, $-\log(p\left(g|f,h\right))$ is defined as $J_{MLEM}(f)$.

$$\begin{aligned}J\left(f\right)&=-\log\left(p\left(f|g,h\right)\right)\\&\propto-\log\left(p\left(g|f,h\right)\right)-\log\left(p\left(f\right)\right)\\&=-\log\left(p\left(g|f,h\right)\right)-\log\left(p_g\left(f\right)\right)-\log\left(p_l\left(f\right)\right)\\&=J_{MLEM}(f)+\int_x\lambda_g|\bigtriangledown f|^\alpha dx\\&\quad+\int_\Phi\lambda_l\|\bigtriangledown f(x)-\bigtriangledown g(x)\|^2dx,\end{aligned} \tag{11}$$

where $J_{MLEM}(f)$ is redefined as:

$$\begin{aligned}J_{MLEM}(f)&=\int_x\left(f*h\right)(x)-g(x)\log\left(f*h\right)(x)\\&\quad+\log\left(g(x)!\right)dx\\&\propto\int_x\left(f*h\right)(x)-g(x)\log\left(f*h\right)(x)dx.\end{aligned} \tag{12}$$

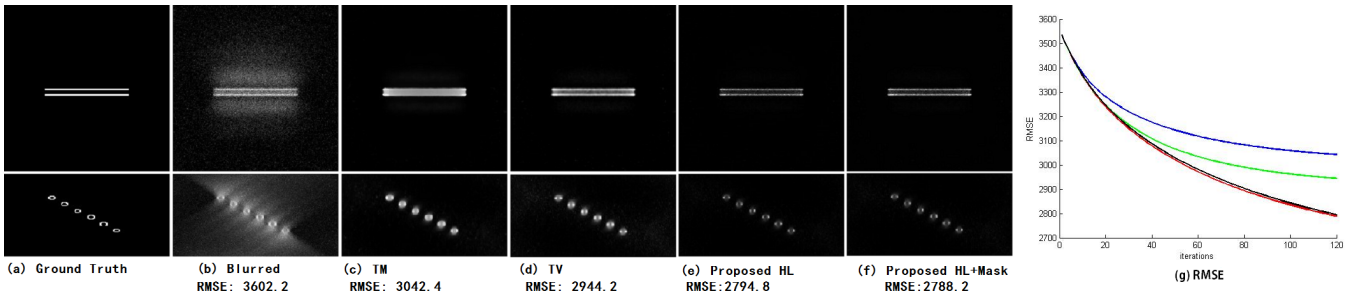

Fig. 3: Deconvolution results of 4 different methods. The top row indicates the central xy-section of the 3D image data, and the bottom row shows the central xz-section. (a): The ground truth data. (b): The blurred images. (c): Result with TM regularization after 120 iterations. (d): Result with TV regularization. (e): Result with the proposed HL. (f): Result with HL+Mask. (g): The trend of the RMSE during iterations (Blue line: TM, Green line: TV, Black line: HL, Red line: HL+Mask).

The derivative of J with respect to f is calculated and set to zero. Then, we obtain a regularized version of the MLEM updating scheme:

$$f_{k+1}(x) = \frac{f_k(x)}{1-\lambda_g\Psi_g-\lambda_l\Psi_l}\cdot[h(-x)*\frac{g(x)}{(f_k*h)(x)}], \tag{13}$$

where $\Psi_g = div(\frac{\bigtriangledown f_k}{|\bigtriangledown f_k|^{2-\alpha}})$ and $\Psi_l = div((\bigtriangledown f_k - \bigtriangledown g)M(x))$ are the regularization terms; λ_g, λ_l are the regularization parameters; div is the divergence, *e.g.*, $div(f) = \bigtriangledown \cdot f$. The iteration process in Equation (13) is implemented in the frequency domain with Fast Fourier Transform (FFT), which extremely improves the computational speed. To find a stop criterion, we calculate the Root Mean Squared Error (RMSE) [14], [15] value in each iteration between the updated latent image and the ground truth. For the real situation, there is no ground truth image, so we calculate the RMSE value between updated latent image and the blurred image. Then, the iteration will be stopped until the changes of the RMSE value is smaller than a small constant value.

C. PSF Modelling

In the updating scheme (13), we assume the PSF (h) is known. However, in the real situation, the true PSF is not given, so we use the VRGL model to produce the PSF. Compared with 2D deblurring, solving the 3D deconvolution problem is more complex and time-consuming. To obtain better results, the precise PSF is needed to avoid losing some useful information during deconvolution process. There are usually three ways to estimate the PSF, namely experimental, analytical and computational methods [26]. Using the experimental method to obtain the PSF usually results in a very poor Signal-to-Noise Ratio (SNR) [7]. In the computational method, such as blind deconvolution, both of the PSF and the latent image are calculated based on the blurred image, and the optimal result is seriously biased by the initial guess of the PSF. An analytical method, *i.e.*, the VRGL model, is used for modelling the PSF in this paper. The VRGL model is designed to estimate the PSF of the microscopy system, which captures the aberration that caused due to variation of refractive index within the thick specimen. The comparison of different PSF models is beyond the scope of this paper, and more details of the VRGL model are explained in [3].

IV. Experiments and Results

To demonstrate the effectiveness of the proposed approach, experiments are conducted using three different datasets, including two synthetic datasets and one real WF Fluorescence Microscopy Zebrafish Embryo dataset. All of the results are evaluated using the Root Mean Squared Error (RMSE) [14], [15], Peak Signal-to-Noise Ratio (PSNR) and Normalized Mean Integrated Squared Error (NMISE). The MAP with global Hyper-Laplacian (HL) and the MAP with Hyper-Laplacian and Local Mask (HL+Mask) are tested, compared with TV and TM regularization methods.

A. Synthetic Data

Two groups of synthetic data are used for testing, including the Hollow Bar and the Hela Cell Nucelus dataset. For the TV and TM regularization methods, the RMSE lines converge after about 120 iterations.

1) Hollow bar: The synthetic hollow bar data are collected from http://bigwww.epfl.ch/deconvolution/?p=bars. The ground truth data are blurred first using a theoretical WF microscopic PSF, and then corrupted by both Gaussian noise and Poisson noise with the signal-to-noise ratio (SNR) of 15dB. Voxel volumes of this dataset are $256 \times 256 \times 128$. Parameters of the synthetic PSF include Numerical Aperture NA= 1.4, spherical aberration W = 0, wavelength λ = 500nm, spatial resolution Δr = 100nm and Axial resolution Δz = 200nm. The best results for TM, TV regularization and proposed method are achieved with regularization parameters $\lambda_{TM} = 3*10^{-7}$, $\lambda_{TV} = 0.001$, $\lambda_g = 0.05$, $\lambda_l = 10^{-8}$ and $\alpha = 1/3$. Results using different methods after 120 iterations are shown in Fig. 3, which illustrates that the two proposed methods have improved the results of TM and TV. The result using the TM regularization is over smooth after 100 iterations, and the regularization term will become larger and larger during iterations. The result of HL+Mask is a little sharper than that of HL. In Fig. 3, the tendency of the RMSE using

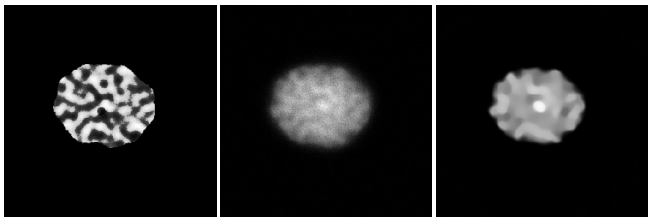

(a) Ground Truth (b) Blurred RMSE:5907.4 (c) TM RMSE:4153.0

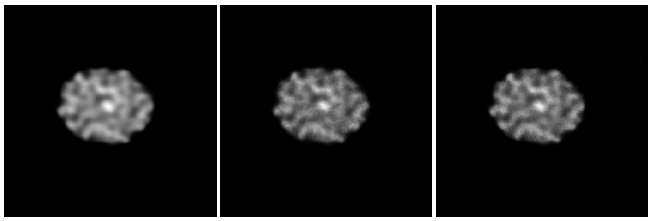

(d) TV RMSE:4081.7 (e) Proposed HL RMSE:4059.9 (f) Proposed HL+Mask RMSE:4052.0

Fig. 4: The HeLa cell dataset results using 4 different methods after 120 iterations.

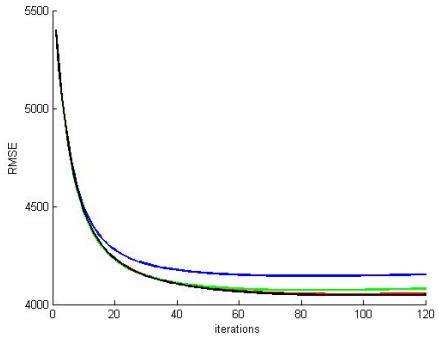

Fig. 5: RMSE results for Hela Cell synthetic data. Blue: TM, Green: TV, Black: Proposed HL, Red: Proposed HL+Mask

TABLE I: Evaluation using 3 different performance metrics

HeLa	Blurred	TM	TV	HL	HL+Mask
RMSE	5907.4	4153.0	4081.7	4059.9	**4052.0**
PSNR	19.149	21.550	21.667	21.751	**21.752**
NMISEC	8439.0	4966.7	4926.7	4878.7	**4875.8**
Bar	Blurred	TM	TV	HL	HL+Mask
RMSE	5907.4	4153.0	4081.7	4059.9	**4052.0**
PSNR	25.4601	26.9703	27.4010	**27.8959**	**27.8921**
NMISEC	3062.2	3042.4	2944.2	2794.8	**2788.2**

4 different methods is shown. The TV and TM methods have already converged after 100 iterations, and the RMSE lines of the two proposed methods are much lower than those of the other two methods after 50 iterations.

2) HeLa Cell Nucleus: The HeLa Cell Nucleus dataset was first used in [14], and the ground truth data were generated using an online simulation tool [27]. The data are corrupted by a WF PSF without aberration, and then the Poisson noise is added. The SNR of the final blurred data is 1.61. The PSF is generated with Numerical Aperture NA= 1.4, wavelength λ = 530nm, spatial resolution Δr = 64.5nm and Axial resolution Δz = 160nm. For this dataset, $\lambda_{TM} = 10^{-5}$, $\lambda_{TV} = 0.005$, $\lambda_g = 0.01$ with $\alpha = 1/3$, $\lambda_l = 10^{-7}$ with $\alpha = 1/3$ are chosen for testing TM, TV, proposed HL and proposed HL+Mask methods, respectively. After 120 iterations, the results and the RMSE are shown in Fig. 4.

The results shown in Fig. 4 are based on 4 different methods after 120 iterations. It can be seen easily that more out-of-focus light is reduced using the proposed methods. The TV regularization method can preserve the edges of the image, but the result is over smooth in the whole image. Fig. 5 illustrates that all of the 4 methods converge after about 60 iterations. After convergence, the RMSE of the results using the proposed methods is lower than that of the TV and TM methods. In Table 1, scores of proposed methods using two other performance metrics, PSNR and NMISEC, are also the best, compared with TV and TM regularization methods.

B. Zebrafish Embryo Data

We collected fluorescent light microscopy images of entire living vertebrates (zebrafish up to 5 days post fertilisation) that contain information on single immune cell types and pathogens in the whole organism. The WF fluorescent zebrafish embryo dataset was recorded by In Cell Analyzer 2000, and the Microscopy type is fluorescence with Numerical Aperture NA = 0.1, Wavelength $\lambda = 490nm$, Spatial resolution Δr = 3.7μm, Axial resolution Δz = 20μm, magnification =2.0, focal length =100μm. The stack size is 2048×2048×41. Parameters for this dataset include $\lambda_{TM} = 5 \times 10^{-5}$, $\lambda_{TV} = 0.01$, $\lambda_g = 0.05$ with $\alpha = 1/3$, $\lambda_l = 10^{-6}$ with $\alpha = 1/3$. There is no corresponding ground truth data for the recorded zebrafish images, so quantitative scores using performance metrics of the final results are not calculated. The qualitative results are shown in Fig. 6, and in Fig. 7, we zoom in on a specific region of the results to get more details. As expected, the proposed HL and HL+Mask methods produce improved results, compared with TM and TV.

V. Conclusion

In this paper, we have proposed a unique deconvolution method for 3D WF microscopy data using the MAP approach with sparse priors. The novelty of the method is that we use the Hyper-Laplacian distribution as a sparse prior to describe the log-gradient distribution, and a local mask is applied to 3D deconvolution for reducing the ringing artifacts. The Hyper-Laplacian distribution is much closer to the log-gradient distribution than other models, especially for WF z-stack images. Results on both synthetic data and real WF fluorescence data from zebrafish embryos show that the proposed methods have potential applicability for 3D WF microscopy images, compared with other methods. Limitations of the proposed methods are that it takes hundreds iterations to obtain a satisfactory result, which is time consuming, and the parameters are not adaptive. Future work will address the issue of the best way to determine the suitable parameters, and

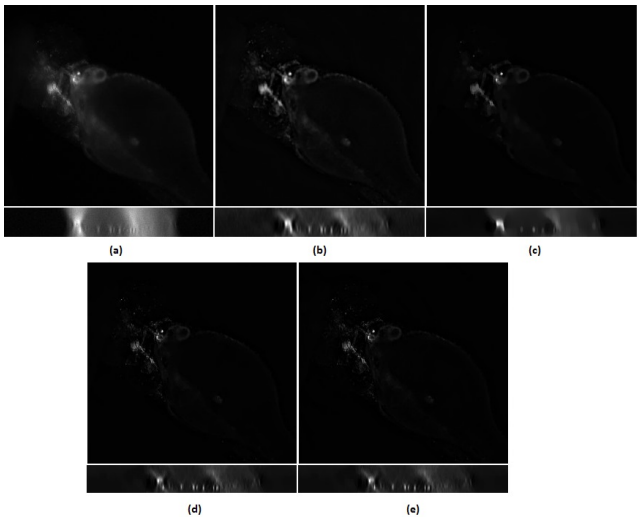

Fig. 6: The Zebrafish data results using 4 different methods. The central xy-section and central xz-section of the z-stack images are shown in each block. (a): Central frame of the Recorded images. (b): TM. (c): TV. (d): Proposed HL. (e): Proposed HL+Mask.

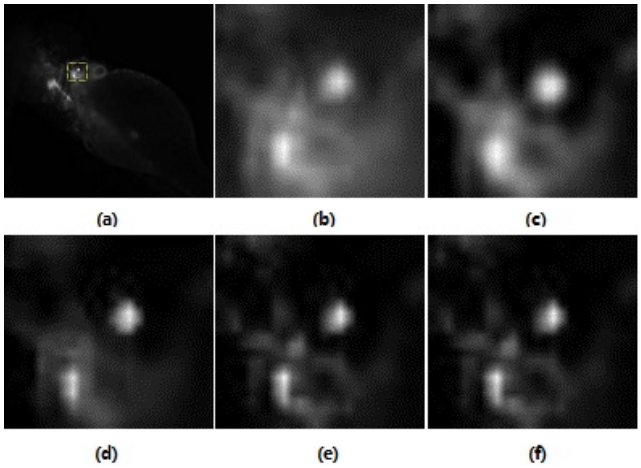

Fig. 7: To observe the results in detail, we magnify the results shown in Fig. 6. (a): Central xy-section with a yellow square. (b): Zoom-in of the yellow square region. (c): TM. (d): TV. (e): Proposed HL. (f): Proposed HL+Mask.

also to improve the computational speed for high throughput image analysis.

REFERENCES

[1] I. T. Young, "Image fidelity: characterizing the imaging transfer function," *Methods Cell Biol*, vol. 30, pp. 1–45, 1989.

[2] P. J. Shaw, "Comparison of widefield/deconvolution and confocal microscopy for three-dimensional imaging," in *Handbook of Biological Confocal Microscopy*. Springer, 2006, pp. 453–467.

[3] S. Hiware, P. Porwal, R. Velmurugan, and S. Chaudhuri, "Modeling of PSF for refractive index variation in fluorescence microscopy," in *IEEE Conference on Image Processing*, 2011, pp. 2037–2040.

[4] M. Bertero, P. Boccacci, G. Desidera, and G. Vicidomini, "Image deblurring with poisson data: from cells to galaxies," *Inverse Problems*, vol. 25, no. 12, p. 123006, 2009.

[5] L. Shao, R. Yan, X. Li, and Y. Liu, "From heuristic optimization to dictionary learning: A review and comprehensive comparison of image denoising algorithms," *IEEE Transactions on Cybernetics*, doi:10.1109/TCYB.2013.2278548.

[6] L. Shao, H. Zhang, and G. de Haan, "An overview and performance evaluation of classification-based least squares trained filters," *IEEE Transactions on Image Processing*, vol. 17, no. 10, pp. 1772–1782, 2008.

[7] J. G. McNally, T. Karpova, J. Cooper, and J. A. Conchello, "Three-dimensional imaging by deconvolution microscopy," *Methods*, vol. 19, no. 3, pp. 373–385, 1999.

[8] A. ĭ. N. Tikhonov, *Numerical Methods for the Solution of Ill-posed Problems*. Springer, 1995, vol. 328.

[9] T. Tommasi, A. Diaspro, and B. Bianco, "3D reconstruction in optical microscopy by a frequency-domain approach," *IEEE Transactions on Signal Processing*, vol. 32, no. 3, pp. 357–366, 1993.

[10] W. H. Richardson, "Bayesian-based iterative method of image restoration," *Journal of the Optical Society of America*, vol. 62, no. 1, pp. 55–59, 1972.

[11] L. Lucy, "An iterative technique for the rectification of observed distributions," *The Astronomical Journal*, vol. 79, p. 745, 1974.

[12] L. A. Shepp and Y. Vardi, "Maximum likelihood reconstruction for emission tomography," *IEEE Transactions on Medical Imaging*, vol. 1, no. 2, pp. 113–122, 1982.

[13] N. Dey, L. Blanc, Feraud, C. Zimmer, P. Roux, Z. Kam, M. Olivo, C. Jean, and J. Zerubia, "Richardson–Lucy algorithm with total variation regularization for 3D confocal microscope deconvolution," *Microscopy Research and Technique*, vol. 69, no. 4, pp. 260–266, 2006.

[14] M. Keuper, T. Schmidt, M. Temerinac Ott, J. Padeken, P. Heun, O. Ronneberger, and T. Brox, "Blind deconvolution of widefield fluorescence microscopic data by regularization of the optical transfer function (OTF)," in *IEEE Conference on Computer Vision and Pattern Recognition*, 2013.

[15] T. Kenig, Z. Kam, and A. Feuer, "Blind image deconvolution using machine learning for three-dimensional microscopy," *IEEE Transactions on Pattern Analysis and Machine Intelligence*, vol. 32, no. 12, pp. 2191–2204, 2010.

[16] A. Levin, Y. Weiss, F. Durand, and W. T. Freeman, "Understanding and evaluating blind deconvolution algorithms," in *IEEE Conference on Computer Vision and Pattern Recognition*, 2009, pp. 1964–1971.

[17] Q. Shan, J. Jia, and A. Agarwala, "High-quality motion deblurring from a single image," *ACM Transactions on Graphics*, vol. 27, no. 3, p. 73, 2008.

[18] D. Krishnan and R. Fergus, "Fast image deconvolution using hyper-laplacian priors," in *Advances in Neural Information Processing Systems*, 2009, pp. 1033–1041.

[19] H. Takeda and P. Milanfar, "Removing motion blur with space-time processing," *IEEE Transactions on Image Processing*, vol. 20, no. 10, pp. 2990–3000, 2011.

[20] J. Portilla, V. Strela, M. J. Wainwright, and E. P. Simoncelli, "Image denoising using scale mixtures of gaussians in the wavelet domain," *IEEE Transactions on Image Processing*, vol. 12, no. 11, pp. 1338–1351, 2003.

[21] A. Levin and Y. Weiss, "User assisted separation of reflections from a single image using a sparsity prior," *IEEE Transactions on Pattern Analysis and Machine Intelligence*, vol. 29, no. 9, pp. 1647–1654, 2007.

[22] M. F. Tappen, B. C. Russell, and W. T. Freeman, "Exploiting the sparse derivative prior for super-resolution and image demosaicing," in *IEEE Workshop on Statistical and Computational Theories of Vision*, 2003.

[23] N. Dey, L. Blanc-Feraud, C. Zimmer, Z. Kam, J.-C. Olivo-Marin, and J. Zerubia, "A deconvolution method for confocal microscopy with total variation regularization," in *IEEE International Symposium on Biomedical Imaging*, 2004, pp. 1223–1226.

[24] C. V. Stewart, "Robust parameter estimation in computer vision," *Society for Industrial and Applied Mathematics Review*, vol. 41, no. 3, pp. 513–537, 1999.

[25] G. Zack, W. Rogers, and S. Latt, "Automatic measurement of sister chromatid exchange frequency." *Journal of Histochemistry and Cytochemistry*, vol. 25, no. 7, pp. 741–753, 1977.

[26] P. Sarder and A. Nehorai, "Deconvolution methods for 3D fluorescence microscopy images," *IEEE Signal Processing Magazine*, vol. 23, no. 3, pp. 32–45, 2006.

[27] D. Svoboda, M. Kozubek, and S. Stejskal, "Generation of digital phantoms of cell nuclei and simulation of image formation in 3D image cytometry," *Cytometry*, vol. 75A, no. 6, pp. 494–509, 2009.